Inorganic Chemistry

pubs.acs.org/IC
Article

Pressure-Induced Comproportionation in Palladium Trifluoride

Sylwia Olszewska, Sharad Babu Pillai, Deepak Upadhyay, Kinga Zdun, Jakub Drapała, Klemen Motaln, Mirela Dragomir, Matic Lozinšek,* and Dominik Kurzydłowski*

Cite This: https://doi.org/10.1021/acs.inorgchem.5c00465

ABSTRACT: Despite its seeming simple stoichiometry, palladium trifluoride (PdF_3) is a mixed-valent system better formulated as $Pd^{II}Pd^{IV}F_6$. In an attempt to verify whether the application of high pressure (P > 1 GPa) might force this compound to form a genuine palladium(III) fluoride ($Pd^{III}F_3$), a joint theoretical and experimental study on its properties at large compression was performed. Indeed, hybrid density functional calculations predict the thermodynamic preference for single-valent (comproportionated) polymorphs at pressures exceeding 30 GPa. The ambient-pressure $LiSbF_6$-type polymorph of $R\bar{3}$ symmetry was experimentally observed to transform into a triclinic $P\bar{1}$ phase above 42 GPa. While this polymorph is still a mixed-valent compound $Pd^{II}Pd^{IV}F_6$, another phase transition, commencing at ∼50 GPa, introduces a monoclinic $C2/c$ phase containing genuine Pd^{III} centers. Both high-pressure polymorphs of palladium trifluoride exhibit novel structure types. Moreover, preliminary data suggest that the $C2/c$ comproportionated structure might host strong one-dimensional antiferromagnetic exchange interactions.

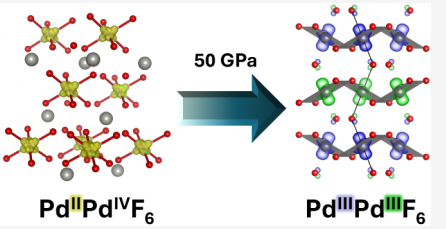

INTRODUCTION

Transition metal compounds offer a versatile platform for studying crucial chemical and physical phenomena, such as electron transfer, metal-to-insulator transition, charge ordering, spin−spin interactions, etc. On the other hand, oxides and fluorides of these elements are materials of immense technological importance, both in current (optoelectronics, photovoltaics) and future (superconductivity, quantum computing) applications. One of the most important characteristics of transition metal compounds is their ability to exhibit a variety of metal oxidation states (electron counts), sometimes within the same crystal structure leading to mixed-valency (charge ordering).[1,2] This process competes with possible metallization and structural distortions, and gaining a deeper understanding of the interplay between charge, spin, and structural ordering is a crucial goal for designing new materials with tailored properties. In this context, AB_3-type compounds are interesting systems due their structural diversity and relation to perovskite (ABX_3) systems.[3]

Pressure, P, as a fundamental thermodynamic variable, can be used to tune the charge-transfer properties in oxides and fluorides.[4−12] Moreover, novel compounds can form at pressures beyond 1 GPa (10 000 bar). While computations suggest that a number of exotic trifluorides, such as CdF_3,[13] HgF_3,[14] BaF_3,[15] might be attained at high pressure experimental verification of these claims is still missing. In fact, in contrast to the well-researched field of pressure-induced phase transitions in rare-earth trifluorides,[7−9] experimental data on the high-pressure phase diagrams of transition metal fluorides is still scarce. Only recently, some light has been shed on this topic with diamond anvil cell (DAC) experiments on fourth period trifluorides (FeF_3,[10,16,17] and MnF_3[11]), as well as that of sixth period (AuF_3).[18]

Herein, a joint computational and experimental study on the high-pressure behavior of palladium trifluoride, a mixed-valent ($Pd^{II}Pd^{IV}F_6$) system which has been proposed to transition into a single-valent $Pd^{III}F_3$ phase upon compression,[19,20] is presented.

RESULTS AND DISCUSSION

The synthesis of palladium trifluoride was first reported by Ruff and Ascher in 1929,[21] and various synthetic paths were reported over the years.[19,20,22−25] Subsequent powder X-ray diffraction (PXRD) investigations assigned it a VF_3-type structure ($R\bar{3}c$ space group) with a single, octahedrally coordinated, Pd site.[26,27] This suggested a single-valent formulation, in which Pd atoms would exhibit the +3 oxidation state. The existence of Pd^{3+} cations, with their formal $4d^7$ electron count, would lead to an uneven occupation of the e_g orbitals of the octahedral [$PdF_{6/2}$] complex, resulting in a Jahn−Teller-type distortion leading to elongation or contraction of the ideal octahedron. However, such a distortion would not be compatible with the high symmetry of the VF_3-type structure. Indeed, a subsequent neutron diffraction study showed that the crystal symmetry is lower ($R\bar{3}$ space group,

Received: January 30, 2025
Revised: April 14, 2025
Accepted: April 17, 2025

Table 1. Properties of the Ground State Structure of Palladium Trifluoride Calculated with the Use of PBE,[33] r^{2}SCAN,[35] and HSE06 Functionals,[36] Compared with Experiments[20,28,29a]

	S.G.	a	α	V	Pd_{1a}–F	Pd_{1b}–F	q_{1a}	q_{1b}	μ_{1a}	μ_{1b}	E_g
PBE	$R\bar{3}c$	5.60	55.66	111.9	2.03		1.6		0.34		0
r^{2}SCAN	$R\bar{3}$	5.53	53.69	102.0	2.10	1.95	1.5	1.8	1.31	0.22	0.6
HSE06	$R\bar{3}$	5.55	54.93	106.4	2.16	1.91	1.5	2.0	1.59	0.07	2.7
Exp.	$R\bar{3}$	5.52(1)	53.90(2)	102.0	2.17	1.90	–	–	1.75	0.00	–

[a]Cell vector (a) for the primitive cell setting and Pd–F distances for 1a and 1b metal sites (Pd_{1a}–F and Pd_{1b}–F) are given in Å, Mulliken charges of Pd atoms (q_{1a}, q_{1b}) in elementary charge (e), cell angle (α) in degrees (°), volume (V) in Å^3, magnetic moments (μ_{1a}, μ_{1b}) in Bohr magnetons (μ_B), the electronic band gap (E_g) in eV. For the $R\bar{3}c$ structure Pd_{1a}–F = Pd_{1b}–F, $q_{1a} = q_{1b}$, and $\mu_{1a} = \mu_{1b}$.

$LiSbF_6$-type structure), with two nonequivalent octahedral Pd sites (Wyckoff positions 1a and 1b) exhibiting markedly different Pd–F distances (2.17 Å for 1a and 1.90 Å for 1b).[28] The $LiSbF_6$-type geometry clearly indicated a mixed-valent formulation with the 1a site occupied by the larger Pd^{2+} cation and the smaller Pd^{4+} ion located on the 1b position. The symmetry around both Wyckoff sites is O_h, and therefore Pd^{2+} ($4d^8$ electron count) should exhibit a high-spin (S = 1) configuration, whereas Pd^{4+} ($4d^6$) should be diamagnetic (S = 0), as in hexafluoropalladates(IV). The existence of such a magnetic arrangement was confirmed by both powder neutron diffraction and magnetic susceptibility measurements.[28,29] Thus, experimental data clearly indicates that at ambient conditions palladium trifluoride is a mixed-valent compound $Pd^{II}Pd^{IV}F_6$, or in short Pd_2F_6, and not $Pd^{III}F_3$. In fact, compounds containing palladium in the +3 oxidation state are much less common than those exhibiting Pd^{II} and Pd^{IV}.[30−32]

DFT Calculations. It is important to note that DFT modeling performed with the use of the generalized-gradient approximation (GGA), in the form of the Perdew–Burke–Ernzerhof (PBE) functional,[33] fails to correctly describe this charge ordering and the resultant magnetic properties, as it yields the single-valent VF_3-type structure ($R\bar{3}c$) as the ground state at ambient pressure.[34] Our PBE calculations confirm this, as we find this polymorph to be 18.6 meV per formula unit (f.u.) lower in energy than the $LiSbF_6$-type one. Within the GGA approximation the $R\bar{3}c$ structure is metallic with small magnetic moment (0.34 μ_B) distributed equally among all Pd sites (Table 1).

In order to attain a better theoretical description of Pd_2F_6, its properties were modeled with the more advanced r^{2}SCAN meta-GGA functional.[35] This approach reduces the difference between experiment and theory yielding the correct $R\bar{3}$ structure as the ground state, with lattice constants very close to the experimental ones (Table 1). This result is in line with previous findings that meta-GGA functionals yield a better description of properties of transition metal compounds.[37,38] However, even at this level of theory, the distinction between Pd^{II}–F (1a) and Pd^{IV}–F (1b) distances is still not as pronounced as in the experimentally determined values. The same applies to the magnetic moment of Pd, which is underestimated for Pd^{II} (μ_{1a}) and overestimated for Pd^{IV} (μ_{1b}).

Only when employing the hybrid HSE06 functional, DFT calculations yield bond lengths and magnetic moments in close agreement with experiment (Table 1). Moreover, the charges on both Pd sites are clearly differentiated, in accordance with the $Pd^{II}Pd^{IV}F_6$ formulation. Finally, both the ferromagnetic ground state of Pd_2F_6 as well as its insulating properties[20] are well reproduced with this DFT functional. This indicates that using this method is essential for the correct description of the mixed-valent nature of palladium trifluoride. It is also noteworthy that the HSE06 functional gives the enthalpy of formation of Pd_2F_6 (−1.36 eV per atom) in close agreement with the experimental value (−1.25 eV per atom).[39] Therefore, a computationally intensive HSE06 method was chosen to perform modeling of the properties of this compound (including the phonon structure and Raman activity).

Electrical measurements performed on Pd_2F_6 compressed to 8 GPa indicated a drastic reduction in resistance upon increase of pressure,[19,20] which led to a hypothesis that Pd^{II}–F and Pd^{IV}–F distances equalize upon compression yielding a genuine Pd^{III} compound ($Pd^{III}F_3$). This interpretation is not supported by the HSE06 calculations, as it is found that at 10 GPa, the two Pd sites in the $LiSbF_6$-type polymorph still have differing Pd–F distances (2.11/1.89 Å), magnetic moments (1.56/0.06 μ_B), and charges (1.4/1.9e). However, these calculations predict that upon compression to 10 GPa the band gap of the $LiSbF_6$-type structure of Pd_2F_6 is reduced by 0.2 eV, which might explain the experimentally observed decrease in resistivity.

The stability of the charge-ordered mixed-valent $R\bar{3}$ structure at modest compression is corroborated by the phase diagram of palladium trifluoride modeled with the quasi-harmonic approximation (QHA) based on HSE06 calculations (Figure 1). The ambient-pressure $LiSbF_6$-type structure remains the most stable polymorph of palladium trifluoride up to 27 GPa, in contrast to previous PBE-calculations which predicted a transition into a tetragonal ($P4_12_12$) metallic polymorph above 19 GPa.[34] In fact, HSE06 calculations indicate that this tetragonal structure is dynamically unstable, i.e., exhibits imaginary modes in the phonon dispersion curves.

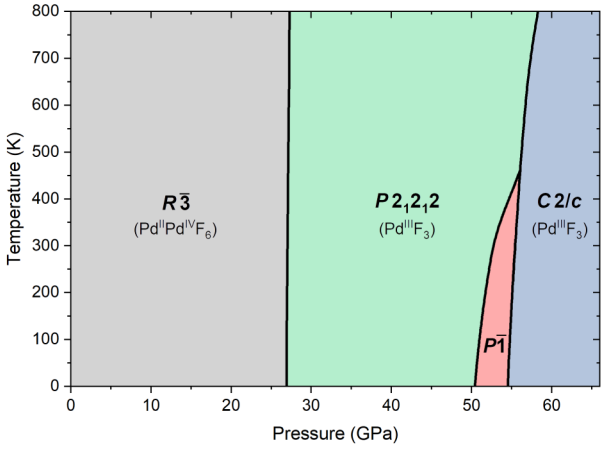

Figure 1. Calculated phase diagram of palladium trifluoride. The black lines mark boundaries between various phases.

https://doi.org/10.1021/acs.inorgchem.5c00465
Inorg. Chem. XXXX, XXX, XXX−XXX

Applying the distortion of one of these modes and reoptimizing the structure yields a orthorhombic structure of $P2_12_12$ symmetry which turns out to be the most stable polymorph up to around 50 GPa (Figure 1). The predicted phase sequence at room temperature and up to 70 GPa is $R\bar{3} \xrightarrow{27\ \text{GPa}} P2_12_12 \xrightarrow{53\ \text{GPa}} P\bar{1} \xrightarrow{55\ \text{GPa}} C2/c$. The triclinic $P\bar{1}$ and monoclinic $C2/c$ structures have been predicted earlier, but with different stability fields.[34]

The analysis of the calculated geometry (see Table S2 for details) and magnetic properties of the $P2_12_12$ and $C2/c$ polymorphs clearly indicates that both contain solely Pd^{3+} cations. First, all Pd sites in these phases, which are computed to be insulators, exhibit the same magnetic moment of 0.6 μ_B (Table 2), in line with the expected value for a spin-1/2 ($4d^7$)

Table 2. Properties of Palladium Trifluoride Polymorphs Calculated at 40 GPa[a]

		q_{Pd}		μ_{Pd}	
$Pd^{II}Pd^{IV}F_6$	$R\bar{3}$	1.4	1.9	1.53	0.04
	$P\bar{1}$	1.4	1.9	1.59	0.07
$Pd^{III}F_3$	$P2_12_12$	1.7		0.65	
	$C2/c$	1.7		0.63	

[a]Mulliken charges of Pd atoms (q_{Pd}) are given in elementary charge, magnetic moments (μ_{Pd}) in μ_B.

Pd^{3+} cation. We note that similar values of the orbital magnetic moment were obtained for related $3d^9$ (La_2CuO_4) and $4d^9$ (AgF_2) spin-1/2 systems.[40−42] Second, the computed charges are equal for all Pd sites, and have values almost exactly in between that of Pd^{2+} and Pd^{4+} cations in $R\bar{3}$. Finally, in both compounds the coordination sphere of palladium takes shape of an elongated octahedron (Figure 2), as expected for a cation with an uneven occupation of the e_g antibonding orbitals.

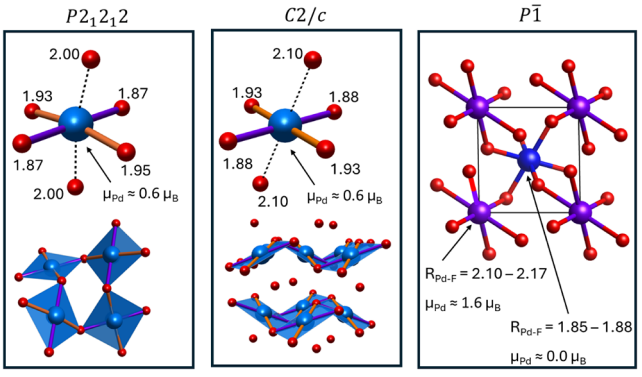

Figure 2. Comparison of the palladium coordination geometry in the $P2_12_12$, $C2/c$, and $P\bar{1}$ polymorphs of PdF_3 computed at 40 GPa. Pd−F distances are given in Å. Violet, light blue, and dark blue atoms denote Pd^{II}, Pd^{III}, and Pd^{IV} sites, respectively, whereas red balls mark F atoms.

Therefore, both the $P2_12_12$ and $C2/c$ polymorph correspond to a single-valent (comproportionated) $Pd^{III}F_3$ formulation. In contrast, the $P\bar{1}$ polymorph exhibits characteristics of a mixed-valent (disproportionated) compound ($Pd^{II}Pd^{IV}F_6$) with an uneven distribution of charges and magnetic moments between Pd atoms, resembling that found in the $R\bar{3}$ structure (Table 2). The general picture emerging from the calculations is a preference for a single Pd^{III} valency in palladium trifluoride for P > 30 GPa, with a very narrow region of stability for the mixed-valent Pd^{II}/Pd^{IV} $P\bar{1}$ polymorph appearing at low temperatures (T < 300 K) between 51 and 54 GPa.

High-Pressure Experiments. In an attempt to verify this prediction experimentally, high-pressure diamond anvil cell (DAC) experiments have been performed on solid palladium trifluoride, measuring in situ Raman scattering and powder X-ray diffraction of this compound compressed up to pressures of 74 and 59 GPa, respectively. Both techniques indicate that the disproportionated $LiSbF_6$-type polymorph is stable at pressures exceeding that of the previous experiment (8 GPa).[19,20] The Raman spectrum collected at 30 GPa agrees well with that obtained by DFT calculations for this phase (Figure 3a), and

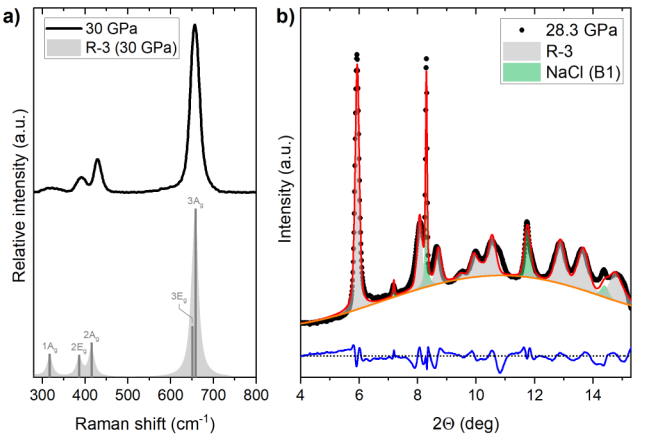

Figure 3. (a) Raman spectrum of powdered palladium trifluoride at 30 GPa (black line) together with that modeled by DFT for the $R\bar{3}$ structure at the same pressure (gray lines). The labels indicate the irreproducible representation of the Raman-active bands, with those of the same symmetry numbered according to their increasing frequency. (b) LeBail fit of the PXRD data (black dots) obtained at 28.3 GPa. Red lines indicate the profile derived from the model incorporating the $R\bar{3}$ polymorph (gray Bragg peaks) and the NaCl pressure marker (green peaks). Blue line gives the difference between model and experiment. The refinement R_{wp} factor is 2.43%.

the PXRD pattern recorded at 28 GPa can be modeled assuming that palladium trifluoride exhibits the $R\bar{3}$ structure (Figure 3b). Importantly, the unit-cell volume obtained through a LeBail fit at this pressure is within 1.4% of that obtained by hybrid DFT modeling. Moreover, below 30 GPa we observe spectral features originating from all of the six Raman-active modes ($3\cdot A_g$ + $3\cdot E_g$) of the $LiSbF_6$-type structure, with only the weakest band, stemming from the $1E_g$ mode, disappearing above 24 GPa (Figure 4).

The $1A_g$, $2A_g$, $2E_g$ modes form three distinct bands visible below 500 cm^{-1}, while the two high-frequency modes ($3E_g$, $3A_g$) form components of a single, and strong, peak located above 600 cm^{-1} (Figure 3a). Importantly, the pressure dependence of the frequencies of all modes is well reproduced by DFT modeling performed for the $LiSbF_6$-type polymorph (Figure 4b).

In contrast to DFT predictions, upon compression above 30 GPa we do not witness a transition from the $R\bar{3}$ polymorph into the $P2_12_12$ structure. Instead, the Raman scattering signature of the $R\bar{3}$ polymorph is observed up to 42 GPa. Only above this pressure we observe indications of a phase change, as the bands originating from $1A_g$, $2A_g$, and $1E_g$ modes disappear and the high-frequency peak broadens into a band that can be described by three components (Figure 4a,b). This

https://doi.org/10.1021/acs.inorgchem.5c00465
Inorg. Chem. XXXX, XXX, XXX−XXX

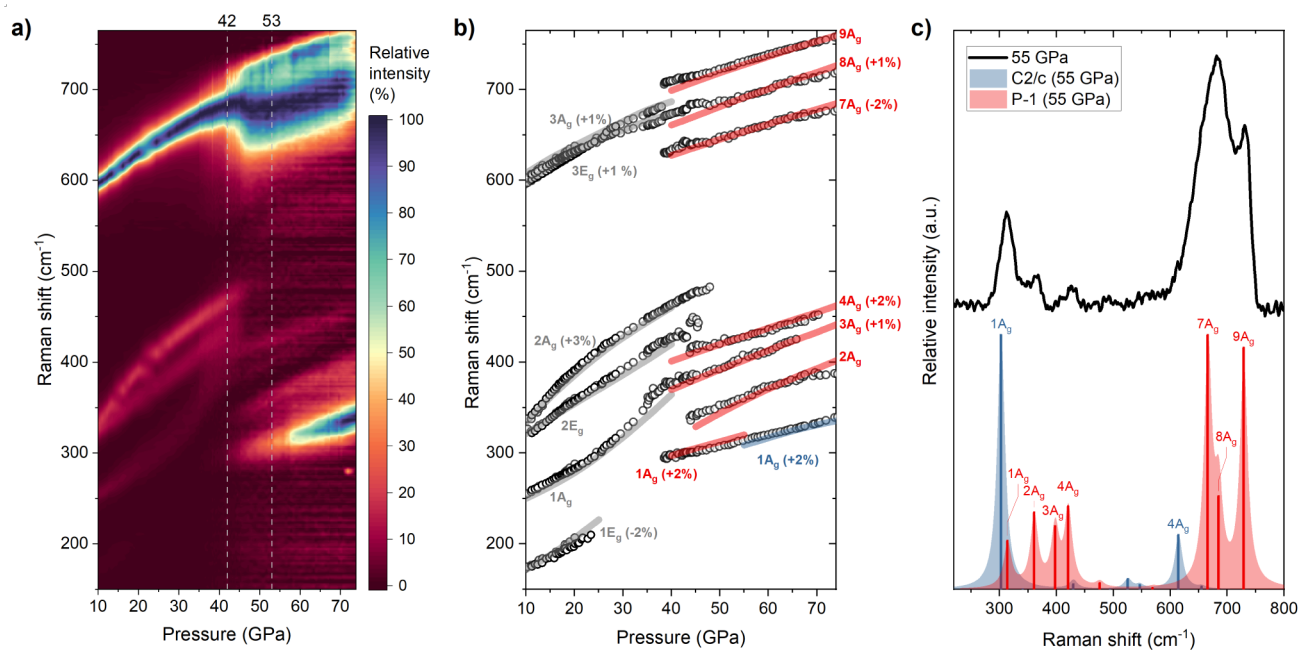

Figure 4. (a) Heat map depicting the evolution of the Raman spectrum of palladium trifluoride upon compression. (b) Pressure dependence of the position of Raman bands: experimental data are given by black circles while the DFT-derived positions of the most intense bands of the $R\bar{3}$, $P\bar{1}$, and $C2/c$ phases are shown by gray, red, and blue lines, respectively. For clarity the frequencies of some modes were scaled, as indicated. (c) Comparison of the experimental (black line) and theoretical (red lines—$P\bar{1}$, blue lines—$C2/c$) Raman spectra at 55 GPa. In (b) and (c) vibrational modes are labeled by their irreproducible representation, those of the same symmetry are numbered according to their increasing frequency.

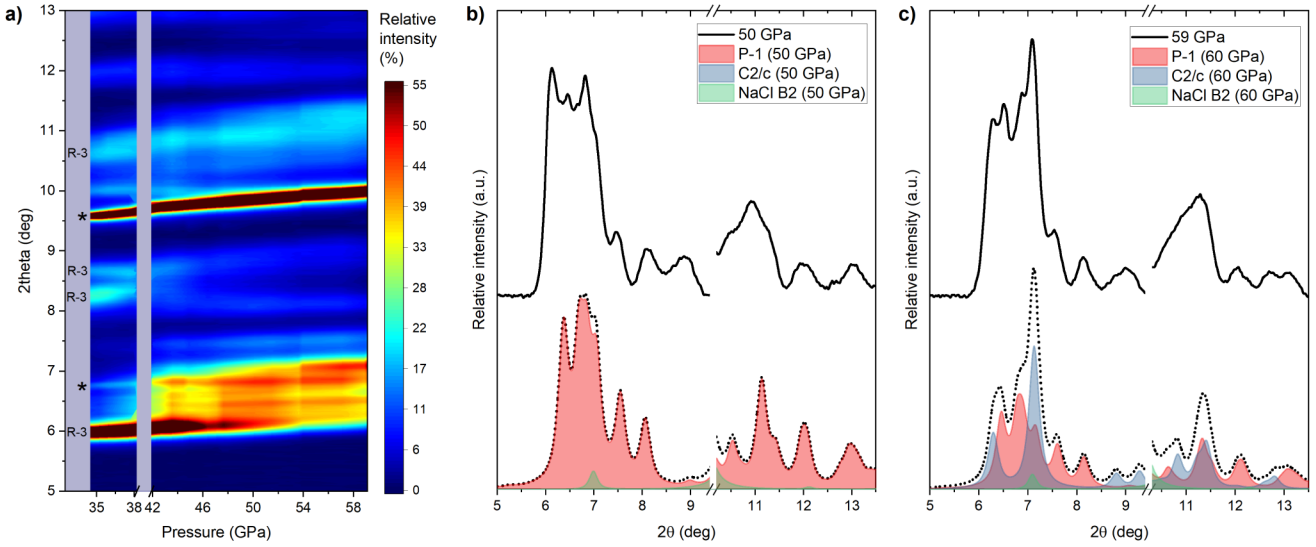

Figure 5. (a) Color map depicting the evolution of the PXRD diffractograms of palladium trifluoride upon compression. Most intense Bragg peaks of the $R\bar{3}$ phase are highlighted together with those originating from the B2 (CsCl) structure of NaCl (marked with an asterisk). PXRD diffractograms collected at (b) 50 GPa and (c) 59 GPa and simulated PXRD patterns for DFT-optimized structures of the $P\bar{1}$ and $C2/c$ polymorphs of palladium trifluoride (red and blue, respectively, a 2:3 molar ration between $P\bar{1}$ and $C2/c$ was assumed in (c)). These diffractograms are summed together with that corresponding to B2 NaCl (green), following its equation of state,[43] to give the simulated dotted black curve. In (b) and (c) the 2θ range in which the strong (110) peak of NaCl is present (9.4−10.4°) has been omitted.

is accompanied by the appearance of four new Raman bands below 500 cm^{-1}, with the intensity of the lowest-frequency one (located at 300 cm^{-1} at 42 GPa) rapidly growing above 53 GPa. At these pressures, this band is assigned to the strongest Raman-active mode $1A_g$ of the $C2/c$ polymorph (Figure 4c), and its emergence interpreted as the sign of palladium trifluoride starting to transition to this structure above 53 GPa. The transition is slow, as the $1A_g$ peak becomes the dominant Raman band only above 71 GPa.

The Raman signature of the phase appearing above 42 GPa, which sluggishly transforms to $C2/c$ above 53 GPa, is matched by that modeled for the $P\bar{1}$ polymorph—both in terms of band position and intensity (Figure 4b,c). Therefore, the picture emerging from Raman scattering measurements is that of the $R\bar{3}$ polymorph transforming abruptly into the $P\bar{1}$ structure at 42 GPa, followed by a sluggish $P\bar{1} \rightarrow C2/c$ phase transformation starting at 53 GPa. All of the three polymorphs are also observed during decompression: the characteristic single-

https://doi.org/10.1021/acs.inorgchem.5c00465
Inorg. Chem. XXXX, XXX, XXX−XXX

band Raman spectrum of $C2/c$ persists down to 43 GPa, and is abruptly replaced at this pressure by the spectrum associated with $P\bar{1}$, which in turns transforms to that of the starting $R\bar{3}$ phase below 18 GPa (Figure S2).

The results of Raman measurements are corroborated by PXRD data in which the disappearance of reflections associated with the $LiSbF_6$ polymorph above 42 GPa is observed (Figure 5a). Unfortunately, the broadening of Bragg peaks upon the phase transition, along with the coexistence and low symmetry of the $P\bar{1}$ and $C2/c$ phases, hindered attempts of obtaining meaningful Rietveld refinements of the experimental data above 42 GPa. However, the PXRD pattern collected at 50 GPa agrees reasonably well with that calculated for the DFT-optimized crystal structure of the $P\bar{1}$ phase (Figure 5b). Moreover, the evolution of the diffractograms at higher pressures, most notably the appearance of a strong Bragg peak at $2\theta = 7.1°$ is consistent with the formation of the $C2/c$ phase, which becomes the main component of the two-polymorph mixture at 59 GPa, as shown in Figure 5c (see also Figure S3). Therefore, both Raman scattering and powder X-ray diffraction measurements indicate that the ambient-pressure $R\bar{3}$ phase transforms to the $P\bar{1}$ structure above 42 GPa, followed by the gradual formation of the $C2/c$ phase at pressures exceeding ~50 GPa.

Room-temperature DAC experiments do not indicate the presence of the $P2_12_12$ phase at any pressure below 74 GPa, in contrast to DFT modeling which predicts it to be the most stable polymorph between 27 and 53 GPa (Figure 1). This discrepancy is most probably due to large energetic barriers associated with the $R\bar{3} \rightarrow P2_12_12$ transition which kinetically hinder its formation. In fact, if one assumes that the $P2_12_12$ is inaccessible due to slow kinetics of its formation, DFT-derived Gibbs free energies (Figure S4) yield the following phase transition sequence at 300 K: $R\bar{3} \xrightarrow{35\ \text{GPa}} P\bar{1} \xrightarrow{55\ \text{GPa}} C2/c$, in close agreement with the one observed in the DAC experiment ($R\bar{3} \xrightarrow{42\ \text{GPa}} P\bar{1} \xrightarrow{50-53\ \text{GPa}} C2/c$). The persistence of some polymorphs beyond the region of their thermodynamic stability, due to large kinetic barriers associated with the phase transitions into thermodynamically favored phases, has also been observed for other fluorides and oxides.[18,44,45]

To the best of our knowledge, both the $P\bar{1}$ and $C2/c$ phases of palladium trifluoride constitute novel structure types, despite being isosymmetric with $CuMoF_6$,[46] and the ambient-pressure structure of MnF_3,[47] respectively. The $C2/c$ structure is also distinct from the YF_3-type structure ($Pnma$) adopted by FeF_3 and MnF_3 at high pressure.[10,11] Additional insights into this phase can be gained from the analysis of the geometry and spin density of the structure obtained from DFT. The four shorter Pd−F contacts of the elongated distorted octahedral coordination sphere of palladium form plaquettes joined into a corrugated sheets of $[PdF_{4/2}]^+$ stoichiometry which are separated by fluorine anions lying in the (100) plane (Figure 6). These anions form two longer Pd−F contacts completing the 6-fold Pd coordination sphere.

Despite the two-dimensional (2D) character of the Pd−F substructure, the spin density has a one-dimensional (1D) distribution, as can be seen in Figure 6. The unpaired electrons reside on a d_{z^2}-like orbital contained in the direction of the longer Pd−F contacts, i.e., the direction of the local z axis of the elongated octahedron, in accordance with what is expected for a d^7 ion. The strong overlap of d_{z^2}-like orbitals of Pd^{3+} cations from successive planes, and the weak interaction of

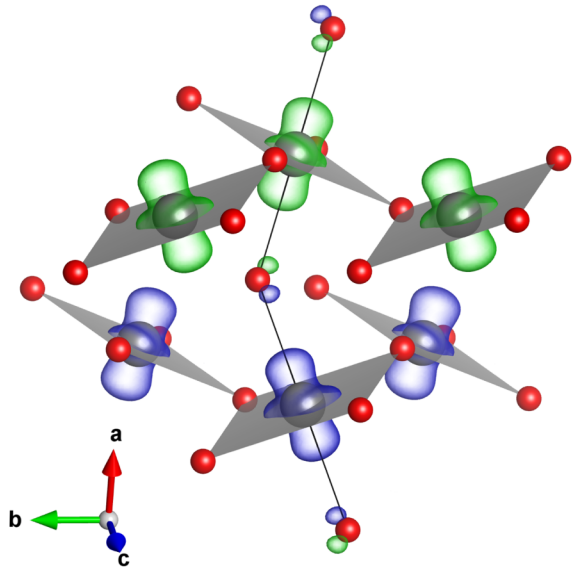

Figure 6. Structure of the $C2/c$ phase of palladium trifluoride (gray and red balls mark Pd and F atoms, respectively). Four shorter Pd−F distances (DFT values at 60 GPa: 2 × 1.87 Å + 2 × 1.91 Å) form a distorted square around Pd (marked with a gray plaquette). The longer Pd−F contacts (2.08 Å) are shown with black lines. Spin-density isosurfaces (drawn at 0.24 $Å^{-3}$) are shown in green/blue for up/down spin density.

cations within the same plane, might lead to strong 1D superexchange interactions, as found in other spin-1/2 systems.[48−52] While a detailed investigation of the strength of various magnetic coupling paths in $C2/c$ PdF_3 is beyond the scope of this study, we note that the difference in DFT-derived energies between the lowest spin state of $C2/c$, characterized by antiferromagnetic (AFM) coupling between $[PdF_{4/2}]^+$ layers (Figure 6), and that of a ferromagnetic solution reaches 135 meV per PdF_3 at 70 GPa. Such a large difference, equivalent to temperatures of 1500 K, hints at very strong interlayer AFM coupling.

CONCLUSIONS

Through a combination of high-level hybrid DFT calculations and DAC experiments we unveil the high-pressure behavior of palladium trifluoride. We show that the computationally intensive hybrid DFT method is essential for the correct description of the mixed-valent (disproportionated) nature ($Pd^{II}Pd^{IV}F_6$) of this compound. The DFT-derived phase diagram indicates the prevalence of comproportionated ($Pd^{III}F_3$) phases, of $P2_12_12$ and $C2/c$ symmetry, at pressures above 27 GPa. In room-temperature DAC experiments, we do not find evidence of formation of the orthorhombic phase, most likely due to the large kinetic barriers associated with its formation. However, both Raman scattering and PXRD *in situ* measurements reveal two other phase transitions: the transformation from the ambient-pressure $R\bar{3}$ structure ($LiSbF_6$-type) into a triclinic phase ($P\bar{1}$) at 42 GPa followed by a sluggish $P\bar{1} \rightarrow C2/c$ transition commencing at about 50 GPa. While palladium trifluoride retains its mixed-valence nature ($Pd^{II}Pd^{IV}F_6$) in the first two phases, the monoclinic polymorph is a genuine $Pd^{III}F_3$ system. Therefore, pressure can drive comproportionation of palladium trifluoride, but this requires greater pressures than previously suggested (50 GPa instead of 8 GPa),[19,20] as well as a phase change from the structure

https://doi.org/10.1021/acs.inorgchem.5c00465
Inorg. Chem. XXXX, XXX, XXX−XXX

observed at ambient conditions. Although the ambient-pressure structure of palladium trifluoride ($R\bar{3}$, $LiSbF_6$-type) is closely related to that of FeF_3 and MnF_3 ($R\bar{3}c$, VF_3-type), both the modeled and observed phase transition sequence reported here greatly differ from that of these two lighter fluorides, which both transform to a YF_3-type polymorph (*Pnma*) upon compression.[10,11] In fact all of the three high-pressure polymorphs of palladium trifluoride ($P2_12_12$, $P\bar{1}$, $C2/c$) studied here seem to be novel structure types, not observed in other systems. Whether these structures are unique for the trifluoride of palladium, or might be observed also in other compounds, such as nickel trifluoride or $CuPdF_6$, remains an open question. Another interesting point for future investigations are the magnetic properties of the $C2/c$ phase. The analysis of the geometry of the superexchange paths in this system, as well as preliminary DFT results, suggest the possibility of very strong and highly anisotropic AFM coupling developing in this phase.

EXPERIMENTAL AND COMPUTATIONAL METHODS

Palladium trifluoride was synthesized by the reaction of elemental fluorine with palladium, following synthetic procedures described in previous studies.[20,25,28] Details of the synthesis and sample characterization at ambient conditions are given in the Supporting Information (Figure S1).

Five high pressure runs were performed with piston–cylinder diamond anvil cells (SymmDAC from Almax easyLab bv, and iBX-80 from DAC Tools LLC) fitted with pairs of low-fluorescence diamonds with culet diameters ranging from 200 to 400 μm. Powdered palladium trifluoride was enclosed in a hole (60 to 150 μm in diameter) made by spark erosion in a stainless-steel gasket preindented to a thickness of 25 to 35 μm. In four runs, the sample was loaded neat into the DAC, whereas in one experiment NaCl was used as a pressure-transmitting medium (PTM)[53] (Figure S5). The results obtained in the runs with and without the PTM were consistent. In Raman scattering experiments pressure was determined from the shift of the first-order Raman signal of the diamond anvil.[54] The spectra were collected at room temperature using an Alpha300M+ confocal microscope (Witec)—for details see Supporting Information. The positions of the Raman bands were determined using the Fityk 1.3.1 software,[55] by fitting the observed bands with pseudo-Voigt profiles. To confirm sample homogeneity, area scans encompassing the whole sample chamber were conducted at selected pressures. High-pressure powder X-ray diffraction measurements were performed at the DanMAX beamline at the MAX IV synchrotron (λ = 0.3542 Å, beam size ~19 × 15 μm^2 with NaCl acting both as the PTM and a pressure gauge.[43] The diffractograms were recorded on a Dectris Pilatus3 X 2M CdTe area detector calibrated with a Si standard. All 2D diffractograms were integrated using the Dioptas software,[56] and subsequent LeBail fit was performed using MAUD.[57] During the refinement, the atomic positions were fixed at values derived from the DFT calculations.

Solid-state spin-polarized density functional theory (DFT) calculations of the geometry and enthalpy of the high-pressure polymorphs of palladium trifluoride were performed with the use of the HSE06 functional,[36] as implemented in the plane-wave VASP 6.4.3 code.[58−60] The cutoff energy of the plane waves was set to 700 eV with a self-consistent field convergence criterion of 10^{-7} eV. The *k*-point mesh was set at $2\pi \times 0.05$ $Å^{-1}$. All structures were optimized using a conjugate gradient algorithm until forces acting on the atoms were less than 5 meV/Å (for more details see Table S1). Geometry optimization was carried out for the lowest energy spin state. This method yielded lattice constants and Pd−F distances of the $LiSbF_6$-type structure of Pd_2F_6 within 2% of those determined experimentally at ambient pressure.[20] The phonon dispersion curves and Raman scattering intensities were calculated using the finite-displacement supercell approach as implemented in the PHONOPY and Phonopy-spectroscopy codes.[61,62] The $P-T$ phase diagram was constructed by comparing Gibbs free energies computed for the various polymorphs under finite temperature conditions using the quasi-harmonic approximation (QHA) implemented in the PHONOPY-QHA script[63] using the Vinet equation of state (EoS).[64] Mulliken gross orbital populations and charges[65] were calculated through the Lobster code (version 5.1.1)[66] by projecting the DFT plane-wave functions onto a localized basis set.

ASSOCIATED CONTENT

Data Availability Statement

The data supporting the findings of this study are available on the Repository for Open Data server (https://repod.icm.edu.pl/) under the DOI number: 10.18150/SG2SSB.

Supporting Information

The Supporting Information is available free of charge at https://pubs.acs.org/doi/10.1021/acs.inorgchem.5c00465.

Details of the Pd_2F_6 synthesis and Raman setup, the room-temperature PXRD diffractogram of Pd_2F_6 synthesized in this study, input files for VASP calculations, structural details of studied phases and comparison of their geometry, Raman spectra upon decompression, evolution of the PXRD diffractograms of palladium trifluoride between 48 and 59 GPa, computed relative Gibbs free energies (PDF)

AUTHOR INFORMATION

Corresponding Authors

Matic Lozinšek − *Jožef Stefan Institute, Ljubljana 1000, Slovenia; Jožef Stefan International Postgraduate School, Ljubljana 1000, Slovenia;* orcid.org/0000-0002-1864-4248; Email: matic.lozinsek@ijs.si

Dominik Kurzydłowski − *Faculty of Mathematics and Natural Sciences, Cardinal Stefan Wyszynski University in Warsaw, Warsaw 01-938, Poland;* orcid.org/0000-0003-2862-0538; Email: d.kurzydlowski@uksw.edu.pl

Authors

Sylwia Olszewska − *Faculty of Mathematics and Natural Sciences, Cardinal Stefan Wyszynski University in Warsaw, Warsaw 01-938, Poland;* orcid.org/0009-0006-2725-4491

Sharad Babu Pillai − *Faculty of Mathematics and Natural Sciences, Cardinal Stefan Wyszynski University in Warsaw, Warsaw 01-938, Poland;* orcid.org/0000-0002-7396-9993

Deepak Upadhyay − *Faculty of Mathematics and Natural Sciences, Cardinal Stefan Wyszynski University in Warsaw, Warsaw 01-938, Poland;* orcid.org/0000-0003-0400-4239

https://doi.org/10.1021/acs.inorgchem.5c00465
Inorg. Chem. XXXX, XXX, XXX−XXX

Kinga Zdun − *Faculty of Mathematics and Natural Sciences, Cardinal Stefan Wyszynski University in Warsaw, Warsaw 01-938, Poland*

Jakub Drapała − *Faculty of Chemistry, Warsaw University of Technology, Warsaw 00-664, Poland*

Klemen Motaln − *Jožef Stefan Institute, Ljubljana 1000, Slovenia; Jožef Stefan International Postgraduate School, Ljubljana 1000, Slovenia;* orcid.org/0000-0003-0051-8611

Mirela Dragomir − *Jožef Stefan Institute, Ljubljana 1000, Slovenia; Jožef Stefan International Postgraduate School, Ljubljana 1000, Slovenia;* orcid.org/0000-0002-4910-253X

Complete contact information is available at: https://pubs.acs.org/10.1021/acs.inorgchem.5c00465

Author Contributions

The manuscript was written through contributions of all authors. All authors have given approval to the final version of the manuscript.

Notes

The authors declare no competing financial interest.

■ ACKNOWLEDGMENTS

The support from the National Science Centre, Poland (NCN) (OPUS Grant UMO-2020/39/I/ST4/03442) and Slovenian Research and Innovation Agency (ARIS) (N1-0225 and P2-0105) in the form of a joint project within the Central European Science Partnership (CEUS); the European Research Council (ERC) under the European Union's Horizon 2020 Research and Innovation Programme (Starting Grant 950625); and the Jožef Stefan Institute Director's Fund is gratefully acknowledged. We acknowledge Polish high-performance computing infrastructure PLGrid for awarding this project access to the LUMI supercomputer, owned by the EuroHPC Joint Undertaking, hosted by CSC (Finland) and the LUMI consortium through PLL/2022/03/016434. The authors acknowledge MAX IV Laboratory for time on beamline DANMAX under Proposal 20231156. Research conducted at MAX IV, a Swedish national user facility, is supported by the Swedish Research council under Contract 2018-07152, the Swedish Governmental Agency for Innovation Systems under Contract 2018-04969, and Formas under Contract 2019-02496. DanMAX is funded by the NUFI Grant No. 4059-00009B.

■ REFERENCES

(1) Bandemehr, J.; Zimmerhofer, F.; Ivlev, S.; Pietzonka, C.; Eklund, K.; Karttunen, A. J.; Huppertz, H.; Kraus, F. Syntheses and Characterization of the Mixed-Valent Manganese(II/III) Fluorides Mn_2F_5 and Mn_3F_8. *Inorg. Chem.* **2021**, *60* (17), 12651−12663.

(2) Belak Vivod, M.; Jagličić, Z.; King, G.; Hansen, T. C.; Lozinšek, M.; Dragomir, M. Mechanochemical Synthesis and Magnetic Properties of the Mixed-Valent Binary Silver(I,II) Fluorides, $Ag^{I}_2Ag^{II}F_4$ and $Ag^{I}Ag^{II}F_3$. *J. Am. Chem. Soc.* **2024**, *146* (44), 30510−30517.

(3) Evans, H. A.; Wu, Y.; Seshadri, R.; Cheetham, A. K. Perovskite-Related ReO_3-Type Structures. *Nat. Rev. Mater.* **2020**, *5* (3), 196−213.

(4) Hou, C. J.; Botana, J.; Zhang, X.; Wang, X.; Miao, M. Pressure-Induced Structural and Valence Transition in AgO. *Phys. Chem. Chem. Phys.* **2016**, *18*, 15322−15326.

(5) Grzelak, A.; Gawraczyński, J.; Jaroń, T.; Somayazulu, M.; Derzsi, M.; Struzhkin, V. V.; Grochala, W. Persistence of Mixed and Non-Intermediate Valence in the High-Pressure Structure of Silver(I,III) Oxide, AgO: A Combined Raman, X-Ray Diffraction (XRD), and Density Functional Theory (DFT) Study. *Inorg. Chem.* **2017**, *56* (10), 5804−5812.

(6) Grzelak, A.; Gawraczyński, J.; Jaroń, T.; Kurzydłowski, D.; Budzianowski, A.; Mazej, Z.; Leszczyński, P. J.; Prakapenka, V. B.; Derzsi, M.; Struzhkin, V. V.; Grochala, W. High-Pressure Behavior of Silver Fluorides up to 40 GPa. *Inorg. Chem.* **2017**, *56* (23), 14651−14661.

(7) Sui, Z.; Wang, J.; Huang, D.; Wang, X.; Dai, R.; Wang, Z.; Zheng, X.; Zhang, Z.; Wu, Q. Orthorhombic-to-Hexagonal Phase Transition of REF_3 (RE = Sm to Lu and Y) under High Pressure. *Inorg. Chem.* **2022**, *61* (39), 15408−15415.

(8) Shao, Z.; Yu, C.; Jin, M.; Wen, J.; Fan, H.; Liu, B.; Zhou, T. Emergence of Diverse Lanthanum Fluorides under High Pressure: From Insulators to Half-Metals and Superconductors. *Phys. Rev. B* **2023**, *108* (6), 064411.

(9) Yan, T.; Zhang, D.; Xi, D.; Zhao, Y.; Wang, C.; Jiang, R.; Xu, Y. Pressure-Induced Structural Phase Transitions and Photoluminescence Properties of Micro/Nanocrystals HoF_3. *Inorg. Chem.* **2024**, *63* (43), 20562−20571.

(10) Lu, W.; Liu, S.; Zhou, M.; Wang, H.; Liu, G.; Liu, H.; Ma, Y. Observation of Iron with Eight Coordination in Iron Trifluoride under High Pressure. *Angew. Chem., Int. Ed.* **2024**, *63* (16), e202319320.

(11) Liu, J.; Zhu, J.; Yu, H.; Yao, A.; Zhang, Z.; Guan, R.; Bao, K.; Cui, T. Structural Phase Transition and Disproportionation of MnF_3 Under High Pressure and High Temperature. *Inorg. Chem.* **2024**, *63* (34), 16114−16119.

(12) Liu, J.; Zhu, J.; Yu, H.; Zhang, Z.; Wu, G.; Yao, A.; Pan, L.; Bao, K.; Cui, T. Structural Phase Transition and Decomposition of XeF_2 under High Pressure and Its Formation of Xe−Xe Covalent Bonds. *Inorg. Chem.* **2024**, *63* (26), 12248−12254.

(13) Lin, J.; Du, X.; Rahm, M.; Yu, H.; Xu, H.; Yang, G. Exploring the Limits of Transition-Metal Fluorination at High Pressures. *Angew. Chem., Int. Ed.* **2020**, *59* (23), 9155−9162.

(14) Botana, J.; Wang, X.; Hou, C.; Yan, D.; Lin, H.; Ma, Y.; Miao, M. Mercury under Pressure Acts as a Transition Metal: Calculated from First Principles. *Angew. Chem., Int. Ed.* **2015**, *54* (32), 9280−9283.

(15) Luo, D.; Wang, Y.; Yang, G.; Ma, Y. Barium in High Oxidation States in Pressure-Stabilized Barium Fluorides. *J. Phys. Chem. C* **2018**, *122* (23), 12448−12453.

(16) Zhu, F.; Lai, X.; Wu, X.; Li, Y.; Qin, S. Experimental and Theoretical Investigation on the Compression Mechanism of FeF_3 up to 62.0 GPa. *Acta Crystallogr., Sect. B: Struct. Sci., Cryst. Eng. Mater.* **2014**, *70* (5), 801−808.

(17) Lin, Y.; Hu, Q.; Zhu, L.; Meng, Y. Structure and Stability of Iron Fluoride at High Pressure−Temperature and Implication for a New Reservoir of Fluorine in the Deep Earth. *Minerals* **2020**, *10* (9), 783.

(18) Kurzydłowski, D.; Kobyakov, S.; Mazej, Z.; Pillai, S. B.; Chakraborty, B.; Jha, P. K. Unexpected Persistence of *cis*-Bridged Chains in Compressed AuF_3. *Chem. Commun.* **2020**, *56* (36), 4902−4905.

(19) Langlais, F.; Demazeau, G.; Portier, J.; Tressaud, A.; Hagenmuller, P. Mise En Evidence Sous Hautes Pressions d'une Transition Electronique Dans Le Fluorure Pd_2F_6. *Solid State Commun.* **1979**, *29* (6), 473−476.

(20) Tressaud, A.; Bartlett, N. Preparation Magnetic Properties, and Pressure-Induced Transitions of Some $M^{II}M^{IV}F_6$ (M^{II}=Ni, Pd, Cu; M^{IV}=Pd, Pt, Sn) Complex Fluorides. *J. Solid State Chem.* **2001**, *162* (2), 333−340.

(21) Ruff, O.; Ascher, E. Die Fluoride Der VIII. Gruppe Des Periodischen Systems. *Z. Anorg. Allg. Chem.* **1929**, *183* (1), 193−213.

(22) Sharpe, A. G. 675. Simple and Complex Fluorides of Some Noble Metals. *J. Chem. Soc.* **1950**, 3444−3450.

(23) Mazej, Z.; Lutar, K.; Žemva, B. Novel Syntheses of Some Binary Fluorides: The Role of Anhydrous Hydrogen Fluoride. *Acta Chim. Slov.* **1999**, *46*, 229−238.
(24) Mazej, Z.; Benkič, P.; Tressaud, A.; Žemva, B. Palladium Chemistry in Anhydrous HF/AsF_5 Superacid Medium. *Eur. J. Inorg. Chem.* **2004**, *2004* (9), 1827−1834.
(25) Tressaud, A. Structural Architecture and Physical Properties of Some Inorganic Fluoride Series: A Review. *J. Fluorine Chem.* **2011**, *132* (10), 651−659.
(26) Ketelaar, J. A. A. Structure of the Trifluorides of Aluminium, Iron, Cobalt, Rhodium, and Palladium. *Nature* **1931**, *128* (3225), 303−303.
(27) Hepworth, M. A.; Jack, K. H.; Peacock, R. D.; Westland, G. J. The Crystal Structures of the Trifluorides of Iron, Cobalt, Ruthenium, Rhodium, Palladium and Iridium. *Acta Crystallogr.* **1957**, *10* (1), 63−69.
(28) Tressaud, A.; Wintenberger, M.; Bartlett, N.; Hagenmuller, P. Détermination de La Structure Cristallographique et Magnétique du "trifluorure de Paladium" $Pd^{II}Pd^{IV}F_6$ par Diffraction Neutronique. *C. R. Acad. Sci. Ser. C* **1976**, *282*, 1069−1072.
(29) Bartlett, N.; Rao, P. R. New Fluorides of Palladium: Palladium(II) Hexafluoropalladate(IV) and Related Compounds and Palladium Tetrafluoride. *Proc. Chem. Soc.* **1964**, 393−394.
(30) Tressaud, A.; Khairoun, S.; Dance, J. M.; Hagenmuller, P. Palladium Compounds with +III Oxidation State. *Z. Anorg. Allg. Chem.* **1984**, *517* (10), 43−58.
(31) Tressaud, A.; Khairoun, S.; Touhara, H.; Watanabe, N. X-Ray Photoelectron Spectroscopy of Palladium Fluorides. *Z. Anorg. Allg. Chem.* **1986**, *540* (9−10), 291−299.
(32) Mirica, L. M.; Khusnutdinova, J. R. Structure and Electronic Properties of Pd(III) Complexes. *Coord. Chem. Rev.* **2013**, *257* (2), 299−314.
(33) Perdew, J. P.; Burke, K.; Ernzerhof, M. Generalized Gradient Approximation Made Simple. *Phys. Rev. Lett.* **1996**, *77* (18), 3865−3868.
(34) Ma, S.; Zhao, L.; Li, S.; Gao, T.; Peng, F. Potential Rules for Stable Transition Metal Hexafluorides with High Oxidation States under High Pressures. *Phys. Chem. Chem. Phys.* **2023**, *25* (9), 6726−6732.
(35) Furness, J. W.; Kaplan, A. D.; Ning, J.; Perdew, J. P.; Sun, J. Accurate and Numerically Efficient r^2SCAN Meta-Generalized Gradient Approximation. *J. Phys. Chem. Lett.* **2020**, *11* (19), 8208−8215.
(36) Krukau, A. V.; Vydrov, O. A.; Izmaylov, A. F.; Scuseria, G. E. Influence of the Exchange Screening Parameter on the Performance of Screened Hybrid Functionals. *J. Chem. Phys.* **2006**, *125* (22), 224106.
(37) Ning, J.; Furness, J. W.; Sun, J. Reliable Lattice Dynamics from an Efficient Density Functional Approximation. *Chem. Mater.* **2022**, *34* (6), 2562−2568.
(38) Tekliye, D. B.; Sai Gautam, G. Accuracy of MetaGGA Functionals in Describing Transition Metal Fluorides. *Phys. Rev. Mater.* **2024**, *8* (9), 093801.
(39) Wijbenga, G.; Johnson, G. K. The Enthalpy of Formation of Palladium(II) Hexafluoropalladate(IV), $Pd(PdF_6)$, by PF_3 Reduction Calorimetry. *J. Chem. Thermodyn.* **1981**, *13* (5), 471−475.
(40) Fischer, P.; Roult, G.; Schwarzenbach, D. Crystal and Magnetic Structure of Silver Difluoride-II. Weak 4d-Ferromagnetism of AgF_2. *J. Phys. Chem. Solids* **1971**, *32* (7), 1641−1647.
(41) Kastner, M. A.; Birgeneau, R.; Shirane, G.; Endoh, Y. Magnetic, Transport, and Optical Properties of Monolayer Copper Oxides. *Rev. Mod. Phys.* **1998**, *70* (3), 897−928.
(42) Gawraczyński, J.; Kurzydłowski, D.; Ewings, R. A.; Bandaru, S.; Gadomski, W.; Mazej, Z.; Ruani, G.; Bergenti, I.; Jaroń, T.; Ozarowski, A.; Hill, S.; Leszczyński, P. J.; Tokár, K.; Derzsi, M.; Barone, P.; Wohlfeld, K.; Lorenzana, J.; Grochala, W. Silver Route to Cuprate Analogs. *Proc. Natl. Acad. Sci. U. S. A.* **2019**, *116* (5), 1495−1500.
(43) Dorogokupets, P. I.; Dewaele, A. Equations of State of MgO, Au, Pt, NaCl-B1, and NaCl-B2: Internally Consistent High-Temperature Pressure Scales. *High Pressure Res.* **2007**, *27* (4), 431−446.
(44) Dutta, R.; Greenberg, E.; Prakapenka, V. B.; Duffy, T. S. Phase Transitions beyond Post-Perovskite in $NaMgF_3$ to 160 GPa. *Proc. Natl. Acad. Sci. U. S. A.* **2019**, *116* (39), 19324−19329.
(45) Kurzydłowski, D.; Kuzovnikov, M. A.; Tkacz, M. High-Pressure Phase Transition of AB_3-Type Compounds: Case of Tellurium Trioxide. *RSC Adv.* **2021**, *11* (24), 14316−14322.
(46) Llorente, S.; Goubard, F.; Gredin, P.; Bizot, D.; Chassaing, J.; Quarton, M. Synthesis and Crystal Structure of $Cu^{II}Mo^{IV}F_6$ and $Cr^{II}Nb^{IV}F_6$ (LT Form). *Z. Anorg. Allg. Chem.* **1998**, *624* (9), 1538−1542.
(47) Bandemehr, J.; Stoll, C.; Heymann, G.; Ivlev, S. I.; Karttunen, A. J.; Conrad, M.; Huppertz, H.; Kraus, F. The Crystal Structure of MnF_3 Revisited. *Z. Anorg. Allg. Chem.* **2020**, *646* (13), 882−888.
(48) Pratt, F. L.; Blundell, S. J.; Lancaster, T.; Baines, C.; Takagi, S. Low-Temperature Spin Diffusion in a Highly Ideal S = 1/2 Heisenberg Antiferromagnetic Chain Studied by Muon Spin Relaxation. *Phys. Rev. Lett.* **2006**, *96* (24), 247203.
(49) Walters, A. C.; Perring, T. G.; Caux, J.-S.; Savici, A. T.; Gu, G. D.; Lee, C.-C.; Ku, W.; Zaliznyak, I. A. Effect of Covalent Bonding on Magnetism and the Missing Neutron Intensity in Copper Oxide Compounds. *Nat. Phys.* **2009**, *5* (12), 867−872.
(50) Li, J.; Xu, L.; Garcia-Fernandez, M.; Nag, A.; Robarts, H. C.; Walters, A. C.; Liu, X.; Zhou, J.; Wohlfeld, K.; Van Den Brink, J.; Ding, H.; Zhou, K. J. Unraveling the Orbital Physics in a Canonical Orbital System $KCuF_3$. *Phys. Rev. Lett.* **2021**, *126* (10), 106401.
(51) Kurzydłowski, D.; Grochala, W. Large Exchange Anisotropy in Quasi-One-Dimensional Spin-1/2 Fluoride Antiferromagnets with a $d(z^2)^1$ Ground State. *Phys. Rev. B* **2017**, *96* (15), 155140.
(52) Wilkinson, J. M.; Blundell, S. J.; Biesenkamp, S.; Braden, M.; Hansen, T. C.; Koteras, K.; Grochala, W.; Barone, P.; Lorenzana, J.; Mazej, Z.; Tavčar, G. Low-Temperature Magnetism of $KAgF_3$. *Phys. Rev. B* **2023**, *107* (14), 144422.
(53) Celeste, A.; Borondics, F.; Capitani, F. Hydrostaticity of Pressure-Transmitting Media for High Pressure Infrared Spectroscopy. *High Pressure Res.* **2019**, *39* (4), 608−618.
(54) Akahama, Y.; Kawamura, H. Pressure Calibration of Diamond Anvil Raman Gauge to 310 GPa. *J. Appl. Phys.* **2006**, *100* (4), 043516.
(55) Wojdyr, M. *Fityk*: A General-Purpose Peak Fitting Program. *J. Appl. Crystallogr.* **2010**, *43* (5), 1126−1128.
(56) Prescher, C.; Prakapenka, V. B. *DIOPTAS*: A Program for Reduction of Two-Dimensional X-Ray Diffraction Data and Data Exploration. *High Pressure Res.* **2015**, *35* (3), 223−230.
(57) Lutterotti, L. Maud: A Rietveld Analysis Program Designed for the Internet and Experiment Integration. *Acta Crystallogr., Sect. A: Found. Adv.* **2000**, *56* (s1), s54−s54.
(58) Kresse, G.; Furthmüller, J. Efficient Iterative Schemes for Ab Initio Total-Energy Calculations Using a Plane-Wave Basis Set. *Phys. Rev. B* **1996**, *54* (16), 11169−11186.
(59) Kresse, G.; Furthmüller, J. Efficiency of Ab-Initio Total Energy Calculations for Metals and Semiconductors Using a Plane-Wave Basis Set. *Comput. Mater. Sci.* **1996**, *6* (1), 15−50.
(60) Kresse, G.; Joubert, D. From Ultrasoft Pseudopotentials to the Projector Augmented-Wave Method. *Phys. Rev. B* **1999**, *59* (3), 1758−1775.
(61) Togo, A.; Tanaka, I. First Principles Phonon Calculations in Materials Science. *Scr. Mater.* **2015**, *108*, 1−5.
(62) Skelton, J. M.; Burton, L. A.; Jackson, A. J.; Oba, F.; Parker, S. C.; Walsh, A. Lattice Dynamics of the Tin Sulphides SnS_2, SnS and Sn_2S_3: Vibrational Spectra and Thermal Transport. *Phys. Chem. Chem. Phys.* **2017**, *19* (19), 12452−12465.
(63) Togo, A.; Chaput, L.; Tanaka, I.; Hug, G. First-Principles Phonon Calculations of Thermal Expansion in Ti_3SiC_2, Ti_3AlC_2, and Ti_3GeC_2. *Phys. Rev. B* **2010**, *81* (17), 174301.
(64) Vinet, P.; Smith, J.; Ferrante, J.; Rose, J. Temperature Effects on the Universal Equation of State of Solids. *Phys. Rev. B* **1987**, *35* (4), 1945−1953.

https://doi.org/10.1021/acs.inorgchem.5c00465
Inorg. Chem. XXXX, XXX, XXX−XXX

(65) Mulliken, R. S. Electronic Population Analysis on LCAO−MO Molecular Wave Functions. I. *J. Chem. Phys.* **1955**, *23* (10), 1833−1840.
(66) Nelson, R.; Ertural, C.; George, J.; Deringer, V. L.; Hautier, G.; Dronskowski, R. LOBSTER: Local Orbital Projections, Atomic Charges, and Chemical-bonding Analysis from Projector-augmented-wave-based Density-functional Theory. *J. Comput. Chem.* **2020**, *41* (21), 1931−1940.

https://doi.org/10.1021/acs.inorgchem.5c00465
Inorg. Chem. XXXX, XXX, XXX−XXX